Physica Medica 51 (2018) 7–12

Contents lists available at ScienceDirect

Physica Medica

journal homepage: www.elsevier.com/locate/ejmp

Original paper

High resolution hard X-ray 3D mapping of a *Macaca fascicularis* eye: A feasibility study without contrast agents

A. Mittone[a,*,1], Y. Ivanishko[b,c,1], S. Kovalev[b,c], P. Lisutina[b,c], M. Lotoshnikov[b,c], S. Tkachev[c], M. Tkacheva[b,c], L. Crippa[d], V. Dmitriev[a,2], A. Bravin[a,2]

[a] European Synchrotron Radiation Facility, ID17 Grenoble, France
[b] Rostov Eye Clinic "InterYUNA", Rostov-on-Don, Russia
[c] Rostov State Medical University, Central Scientific Research Laboratory, Rostov-on-Don, Russia
[d] Istovet, Laboratorio di Analisi Istopatologiche Veterinarie e Servizi per la Ricerca Scientifica, Besana Brianza, Italy

ARTICLE INFO

Keywords:
Ophthalmology
Eye
Three-dimensional micro-tomography
X-ray phase-contrast imaging
Propagation-based imaging

ABSTRACT

Several complementary methods able to visualize the internal structures of eyes are used in the clinical practice in the diagnosis of pathologies affecting a specific zone of the eye. Despite the significant technological progress, the visualization of the entire eyeball at micrometric resolution is yet an unsolved task both in clinical diagnostics and in laboratory research. With this respect, high resolution 3D images of the eyeball would be extremely useful, in the study of various pathologies of the retina, the lens, and of the optic nerve. In this work we combined the state-of-the-art of micro computed tomography technology with phase-contrast imaging, a recent highly sensitive technique well adapted to investigate soft tissues without the use of contrast agents; we applied the technique in the post-mortem analysis of monkey eyes, which share several similitudes with the human organ. We reported here vascular, nervous and anatomical details of monkey eyes imaged with a $3.1 \times 3.1 \times 3.1\ \mu m^3$ voxel size as well as the first 3D visualisation of the entire globe of Macaca's fascicularis eye. Results have also been compared with, and validated by, histological analysis.

1. Introduction

The clinical procedures for the visualization of the internal structures of eyes include several complementary techniques like biomicroscopy, optical coherence tomography (OCT, [1]), confocal scanning laser ophthalmoscopy (cSLO, [2]), ultrasound scanning in the A- and B-mode (A- and B-scan), as well as ultrasound biomicroscopy (UBM), X-ray micro-computed tomography (X-ray microCT, [3]) and magnetic resonance imaging (MRI). A detailed description of all these techniques can be found in [4]. A complementary method to analyse tissues at (sub)microscopic resolutions is the histological analysis; however this procedure is destructive and is only carried out on excised organs ex-vivo. Moreover, during the preparation process, tissues can be altered by mechanical actions and chemical reagents, with consequent modification of their anatomy. Each clinical imaging method is particularly suited in the diagnosis of pathologies affecting a specific zone of the eye; all methods also present specific requirements for their application. In fact, both OCT and cSLO require a high optical transparency of the sample and can be used in the study of structures in the anterior segment of the eye or in the fundus. The application of UBM is instead limited to the cornea and the anterior chamber angle. B-scan, X-ray microCT and MRI have no optical transparency requirements and are the only techniques potentially allowing the visualization of the entire eyeball. Unfortunately, the resolution of the clinically available instruments, always exceeding 100 µm, is far from that necessary to provide a diagnostically significant image quality of the eye. High resolution images (particularly the ones that show cellular structure of tissue) of the eyeball would be extremely useful even in preclinical trials in the study of different pathologies of the retina, the lens and of the other structures including the optic nerve.

In order to overcome the present limitations encountered by preclinical ophthalmological research a completely different approach has been recently developed in laboratories. It consists in recording the phase variations of X-rays passing through the matter; this signal adds to the weak absorption signal always present in the images [5–7] and does not require the use of additional contrast agents. For a more detailed description of the technique we refer to the Material and Methods section.

* Corresponding author.
E-mail address: alberto.mittone@esrf.fr (A. Mittone).
[1] Authors have equally contributed to the manuscript.
[2] Authors have equally coordinated the project.

https://doi.org/10.1016/j.ejmp.2018.06.004
Received 30 March 2018; Received in revised form 28 May 2018; Accepted 2 June 2018

To our best knowledge, there are only four works in the literature describing the post-mortem application of X-ray to eye imaging either in radiography [8] or using microCT [9–11].

Kelly et al. [8] reported on the results of the study of formalin-fixed porcine eyes using a phase-contrast imaging technique. All images were acquired in radiographic mode, which suffers from structure overlap and does not allow a high resolution discrimination of the tissues. This was a seminal work, demonstrating the interest of applying the phase-contrast imaging techniques in the study of the eye anatomy. Yin et al. (in Chinese) [9] also discussed the use of phase-contrast imaging applied to the post-mortem visualization of the internal structures of New Zealand rabbit eye by microCT; the short paper does not report any detailed anatomical description of the findings. In the work of Hoshino et al. [10] the analysis focus on the optical properties of the eye lenses for different animal species by mean of Talbot interferometry. In the article of Ivanishko et al. [11], the results of 3D intra-cranial computed tomography of rabbit eyes has been reported; however no comparison with respect to histological data is reported. In this work we applied the state of the art high resolution microCT using monochromatic X-rays and the state of the art phase-contrast imaging data reconstruction methods we have developed in the past years [5,12–14].

We present here a full 3D acquisition of formalin-fixed monkey eyes (*Macaca fascicularis*) enucleated post-mortem from adult specimens at an isotropic voxel size of 3.1 μm^3. The results presented here aim at providing for the first time a high resolution 3D model of a monkey eye anatomy, showing the potential of phase-contrast imaging as a complementary preclinical diagnostic technique applied to the vision organ.

2. Methods

2.1. Phase-contrast imaging

In life sciences, samples consist very often of weakly absorbing tissues and structures composed by low Z elements (< 20). For such materials, the sensitivity of conventional radiography drastically decreases because of the small differences (few percent) in the X-ray absorption coefficients of the elements composing the different tissues (NIST database [15]).

The use of contrast agents, like iodine or gadolinium, both injected in vivo, can enhance the contrast generated by the vascular system; tissues can also be marked post-mortem using specific commercial markers or other heavy metal-based dyes [16]. A 3D imaging method able to image full organs at resolutions able to discriminate the smallest capillaries and/or the neuronal morphology, without the injection of invasive contrast agent (in vivo), or without applying an aggressive tissue preparation (post-mortem), is still required [17].

X-ray phase contrast imaging represents a novel way to overcome the limitations of conventional absorption-based imaging without the need of contrast agents. The behaviour of X-rays as they travel through an object can be described in terms of a complex index of refraction defined as $n = 1-\delta + i\beta$, whose real part, δ, and the imaginary part, β, are related to the X-ray phase shifts and attenuation in the object, respectively.

In the energy range typically used in X-ray diagnostics (15–100 keV), the phase term is orders of magnitude higher than the absorption one [18]; therefore radiographic techniques sensitive to variations of the δ term may potentially provide an increased image contrast with respect to those methods based only on the X-ray absorption process [6].

Several techniques have been developed for exploiting the phase effects in X-ray imaging. They include the propagation-based imaging technique (PBI) [19–21], the analyzer-based imaging technique [22,23], the grating interferometric [24,25] and the grating non-interferometric methods [26–28]. All modalities have been widely used in preclinical X-ray radiology; an extensive review of the theoretical basis, of the required technology as well as example of the application in different fields of medicine can be found in [6,29].

The phase-contrast technique applied in this study was the PBI, which makes use of a highly spatially coherent and quasi-monochromatic X-ray beam. Briefly, the X-ray wavefront distorted by traversing a sample, generate characteristic interference patters; at well determined directions, described by the Fresnel diffraction [30], these distortions are transformed in detectable intensity variations that can be recorded by a detector placed at a convenient distance from the sample [19,21]. These intensity variations highlight the borders of the sample or of the details embedded in the sample itself, therefore enhancing their visibility.

2.2. Experimental setup

The experiment was carried out at ID17 BioMedical beamline at European Synchrotron Radiation Facility (ESRF, France). A quasi-monochromatic ($\Delta E/E \sim 10^{-4}$) and quasi-parallel X-ray wave (divergence $< = 1$ mrad horizontally, and $\ll 0.1$ mrad, vertically) beam (energy 35 keV) was selected using a Si(1 1 1) double Laue crystal from a beam produced by a 21-pole wiggler [31]. The propagation distance between the sample and the detector was 11 m. The detection system was composed by a 350 μm thick YAG scintillator screen coupled with a 1:2× optics and a Scientific Complementary Metal-Oxide Semiconductor (sCMOS) PCO edge 5.5 camera [32]. The final pixel size was of 3.1 × 3.1 μm^2. In order to evaluate the real spatial resolution at which the images are obtained it is necessary the knowledge of the Modulation Transfer Function of the detection system. Previous measurements, reported in [32] show that the system used in this work shows an effective spatial resolution of about 8 μm.

2.3. Image acquisition and reconstruction

The computed tomography (CT) was performed by acquiring 5000 angular projections over 2π. Each angular projection presents an exposure time of 0.4 s. Due to the limited ID17 vertical beam size (7 mm) three different CTs were performed at different heights of the organ to acquire the whole volume. The overall image acquisition of a single vertical step lasted about 1 h; such long image acquisition time was linked to an un-optimized methodology applied in this pilot study.

However, as also reported in the discussion section, a fast acquisition procedure can be applied to reduce the acquisition time down to ~2 min for a single tomographic vertical step, without a significant loss of information in the regions of interest. Such times have been achieved by reducing the number of angular projections to 500 with an integration time of 0.1 s.

The extraction of the phase information was performed using the quasi-particle phase-retrieval approach described in [33,34]. The filtered-back projection algorithm [35] was then applied to perform the tomographic reconstruction and to create the 3D volume.

For histopathological examination, samples fixed in 10% neutral buffered formalin (NBF) for 24–48 h, were processed with a Tissue Processor Leica ASP300 S, and paraffin embedded (Embedding Center Leica EG1160). Four micron thick sections were cut, stained with Haematoxylin-Eosin (H&E) and evaluated under a light microscope (Leica DM 2500). Representative images were captured with a digital camera (Leica DFC310 FX).

2.4. Samples and ethical statement

In this experiment we used four formaline-fixed monkey eyes enucleated from adult (4–5 years old) *Macaca fascicularis*. During the imaging procedure the samples were embedded in an agar-agar preparation and included in a transparent cylindrical plastic container of 3 cm in diameter. The average diameter of the eye inside the container was about 1.5 cm. Samples did not undergo any other specific preparation and, in particular, were not in contact with any contrast agent

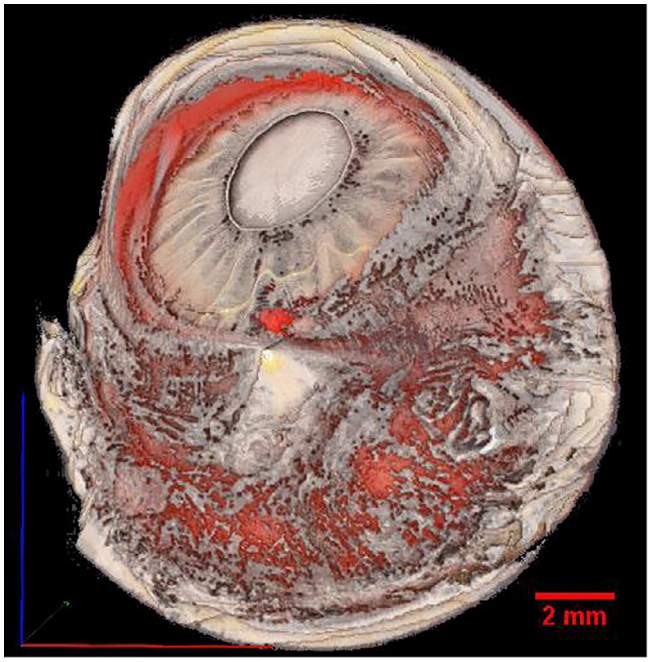

Fig. 1. 3D rendering of one of the imaged eyes. The representation of the whole volume was obtained after binning the original dataset by a factor of 20. In the first plane there is the frontal region of the eye, showing the iris, pupil and lens. The central width of the organ is ~15 mm.

neither in vivo nor post-mortem. Samples were provided by the CEA-Leti/Clinatec, Institute (Grenoble, France) from animals sacrificed within other experimental protocols. No live animals were used for this experiment or sacrificed for the aim of this study.

3. Results

The 3D reconstruction of the eye allows visualizing the smallest internal structure details thanks to the high image contrast provided by the PBI method. The rendering of one of the eye is reported in Fig. 1. It has been obtained using the software Amira 6.2 (FEI), after an isotropic binning of the original data; the application of binning was mandatory, because a single dataset is as large as ~600 Gb.

Separate 3D volume sections extracted from the high resolution unbinned volume are reported in Fig. 2. Fig. 2a shows a frontal section of the optic nerve at the point of its entry into the eyeball with an enhanced visualization of the choroidal vessels. Fig. 2b shows the same area in the sagittal plane. The optic nerve, its fibers and vessels, the perineural space, the place of perforation of sclera by the optic nerve, the choroid, and detached retina fixed to the optic disk are all perfectly depicted. On the retina, more layers are distinguishable, which are characterized by varying reflectivity; because of the postmortem tissue degradation and of the anatomical changes due to the formalin fixation, a comparison of these images with the results of the application of intravital methods on the same samples would be meaningless (and it is outside the purpose of this pilot work).

Fig. 2c shows the optic nerve cross-section (diameter ~3.1 mm) a few (2–4) millimetres posterior to the eyeball. We can observe the central artery and vein, bundles of nerve fibers and the optic nerve sheathes. Rounded black formations around the nerve correspond to air bubbles embedded in the agar-agar. Fig. 2d shows detailed cross-section of the optic nerve in the frontal plane at the point of its entry into the eyeball. Of particular significance is the extremely detailed depiction of the optic disc and of the cribriform plate.

Fig. 3 reports a cross-section of the eyeball; we can appreciate the lens with the capsule, the iris with the pupil and ciliary processes of the ciliary body. Moreover, in the area called anterior chamber angle, the Schlemm's canal (scleral venous sinus of the eye) is visible. The total retinal detachment is instead a clear sign of postmortem degeneration.

In Fig. 4 the preliminary result of a scan performed in ~2 min using only 500 projections (integration time: 0.1 s per angular view) are shown. Some artefacts appear in the images: they are generated by the strong undersampling in terms of angular projections as well as by the higher overall noise due to the reduced exposure time. However, these artefacts do not obscure any of the features of interest, as reported in image 4b. Image 4 has been obtained at a reduced radiation delivered and acquisition time with respect to the images presented in Figs. 2 and 3 (reduction factor ~40).

Fig. 5 reports the comparison of the CT slice of the onset of the optic nerve (a), of the retina (b) and of the ciliary processes of the ciliary body (c) with the corresponding histological sections. The CT images contain the anatomical information present in the histological slices with similar resolution. The anatomical differences are ascribed to the not perfect matching of the location of the image with the histology. These results, even if limited to four samples, provide an exhaustive overview of the performances of high resolution phase-contrast CT to represent the main anatomical, vascular, and nervous features of the eye ball.

The images here reported refer to one single eye (left eye); nonetheless similar results in term of quality and depiction of structures have been obtained with all our datasets; results are not reported to avoid unnecessary duplication.

Measurements of the incident photon flux at the sample position have been performed prior to the experiment. The dose delivered during the scans has been calculated by means of Monte Carlo simulations using the method proposed in [36]. The results of the simulations indicate an average dose of ~49.2 Gy for the scans performed using 5000 angular projections. The dose delivered is reduced to ~1.2 Gy in case of the fast scans (500 projections and shorter integration times). Besides these values greatly exceed the clinical standards, they are still sufficiently low to avoid structural changes within the organ and therefore suitable for ex-vivo preclinical studies. It must be highlighted that the dose reduction was outside the scope of this pilot and demonstrative work.

4. Discussion and conclusions

In this work, we report the results of the visualization of the 3D structure of a primate eyeball obtained using an X-ray computed tomography imaging technique without the use of contrast agents. Images show an unprecedented spatial resolution and high contrast, thanks to the application of the PBI technique. This imaging modality has been already validated by our team in ex-vivo and preclinical research of various pathologies of the breast [5], spinal cord [13,37] and cartilage [12]. However some aspects must be still improved and developed for future broader application in ophthalmology. First, the long acquisition time, and therefore high doses delivered, required to obtain Figs. 1–3, which was as long as ~3 h (5000 projections, 0.4 s of integration time, 3 vertical CT steps). Preliminary results of time reduction down to few minutes to image the whole volume (500 projections, 0.1 s of integration time) are reported in Fig. 4. It shows that such reduction does not compromise the diagnostic significance of the images: despite the appearance of some artefacts due to the data undersampling and a higher noise level, the general image quality is preserved and, most importantly, all ultrastructure the structural details of nerve fibers and the nerve sheathes are fully visible.

The long integration time of the here presented images is the consequence of the extremely high spatial resolution of the detection system, which is at the cutting edge of the present technology to image an entire eye. In order to obtain the same image quality (same statistics per pixel) with another pixel size, it should be considered that the integration time increases with the inverse of the square of the pixel size. In order to reduce the acquisition time and dose delivered, several

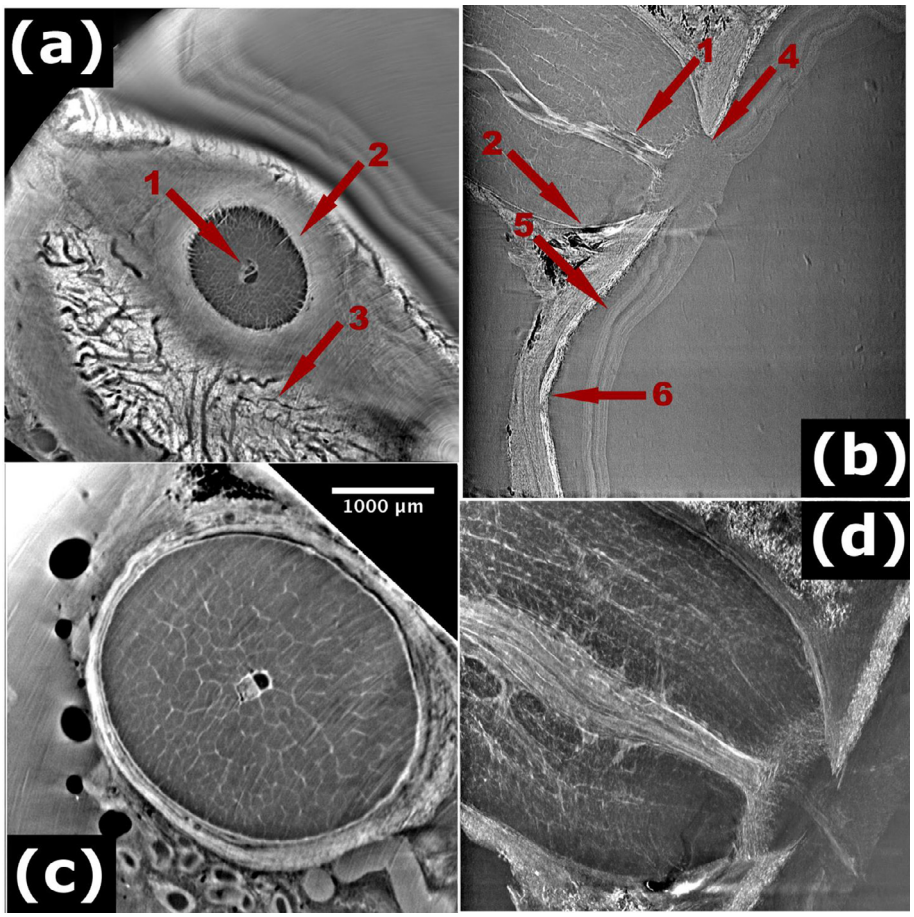

Fig. 2. (a) Frontal view of the insertion region of the optic nerve; (b) Sagittal view of the optic nerve insertion; (c) Frontal view of the optic nerve; (d) Detailed sagittal view of the optic nerve and of the lamina cribrosa. (1) Central artery and vein of the retina; (2) Optic nerve sheath; (3) Vessels of the choroidea; (4) Lamina cribosa (area of the optic nerve insertion); (5) Detached retina; (6) Choroid and sclera.

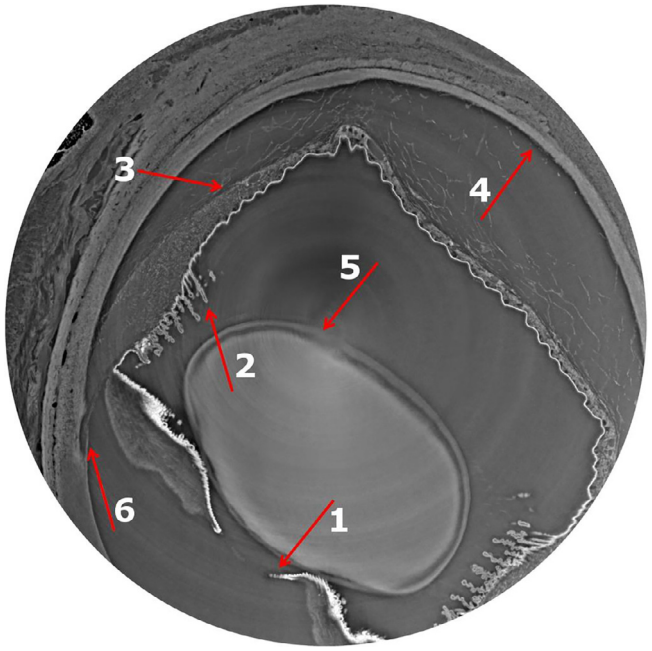

Fig. 3. Cross-section of the monkey eye, centered on the lens. (1) the pupil and pupillary zone of the iris; (2) ciliary processes of the ciliary body; (3) detached retina; (4) sclera; (5) lens; (6) Schlemm's canal. The central part of the image look slightly blurred due to the ring artifact correction applied.

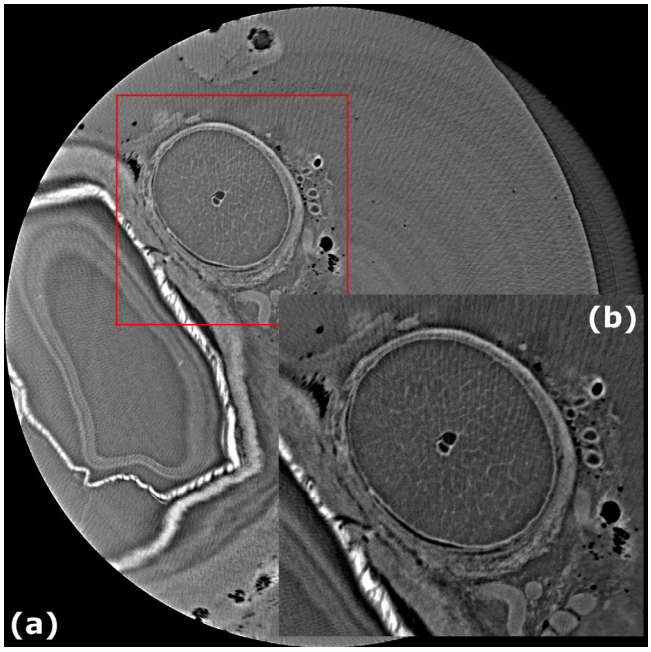

Fig. 4. Preliminary results obtained with a fast scan. (a) Overview of the whole region, (b) magnified region indicated by the red square of figure (a). The external black regions, on the right of image (b) are air bubbles present in the agar-agar medium.

strategies could be adopted, for instance the use of a detection system more efficient of the here described, like a single photon counting. Unfortunately, such detectors (ex: Maxipix, described in [38]) are not yet available with pixels size smaller than 50 µm. Therefore the only way to use them in a high resolution application is to include in the setup a divergent X-ray optical system, able to magnify the image

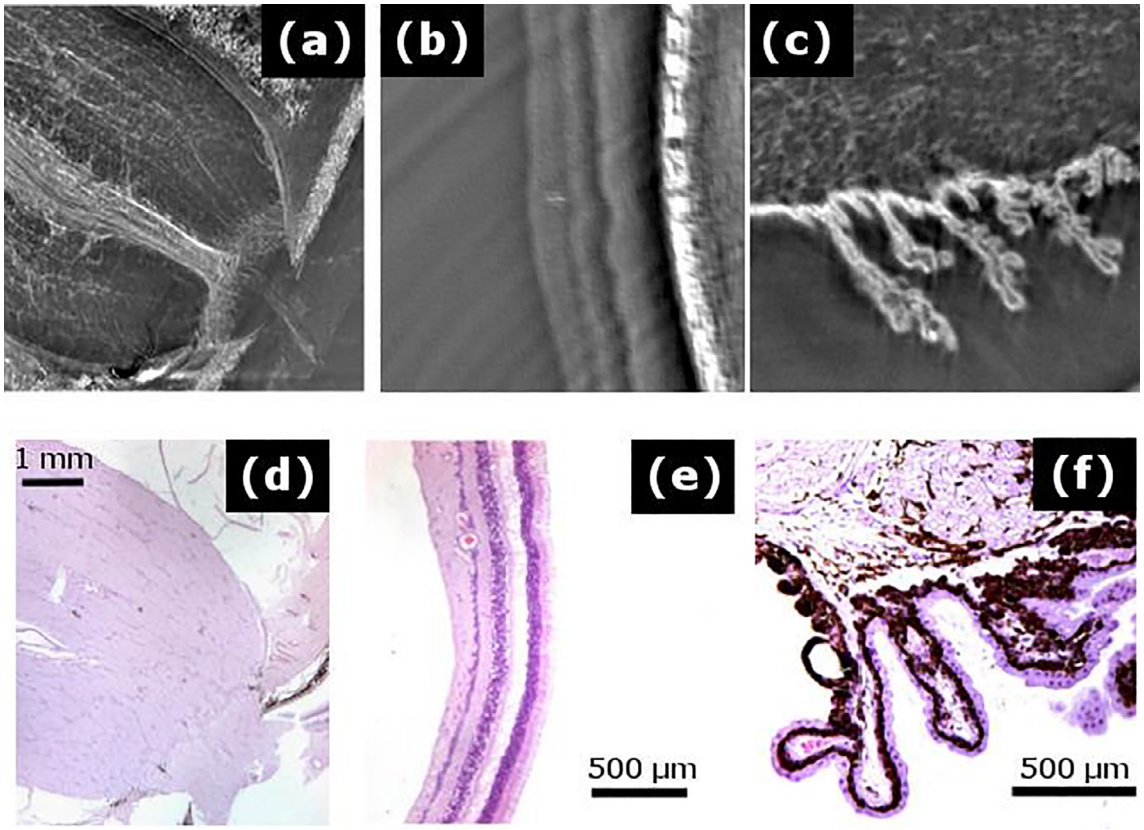

Fig. 5. Comparison of phase contrast imaging with histology (H&E staining). (a)–(c) sub-regions obtained using phase-contrast imaging. (d)–(f) histological results. The images used for the comparison do not represent exactly the same sections. (a), (d) onset of the optic nerve; (b), (e) retina; (c), (f) ciliary processes of the ciliary body.

before acquisition.

Another possibility in reducing the total time consists in limiting the number of acquired angular projections, to be then processed using iterative reconstruction algorithms like Equally Sloped Tomography (EST) [39]. It has been already shown that this algorithm allows obtaining CT images of equivalent noise using 4 times less projections. By implementing these technical modifications, the total imaging time might be reduced down to a few minutes, which is compatible with a preclinical in vivo work on animal models.

One more possibility in reducing the acquisition time is given by the spiral CT [40] modality of data acquisition.

The vertical beam size used here represents also a limitation if the whole eye has to be imaged. In fact, three CT at different sample heights were needed to acquire the data necessary to visualize the whole volume. In most of practical cases, however, only a certain region of the eye needs to be investigated, thus reducing the problem of this vertical stitching.

If we consider only the problem of a reduction of the image acquisition time, a suitable alternative is provided by a polychromatic X-ray spectrum instead of the monochromatic radiation; a pink beam setup is available at different SR facilities (SLS, LNLS) [41,42] as well at the ID17 and ID19 beamlines at the ESRF. At ID17 the pink beam facility provides an intense beam, suitable for high resolution imaging, in the energy range (25–70 keV). This modality will be employed in our planned tomographic scans of different regions of the eye using submicrometric pixel sizes, to better characterize the vascular and neuronal network.

Some artefacts are visible in the Figs. 3 and 5; in particular in the pupillary region (Fig. 3, label 1) and in the ciliary body (Fig. 5c). These artefacts are related to the sample drying out during the image acquisition. Considering the anatomy of our object, these artefacts, and especially the rings, do not represent a limitation in the image interpretation because are located outside of the region where the features of interested are located. Furthermore, faster acquisition will contribute to reduce these artefacts, especially the ones related to the drying of the sample.

In conclusion, this pilot study show the potential of using high resolution X-ray CT imaging in the 3D visualization of the internal structures of primate eyes. We have discussed the further technical developments necessary to further enhance the significance of the images, also because only the in vivo application could provide functional information in addition to the anatomical one.

Acknowledgments

We acknowledge CEA-Leti/Clinatec, Grenoble, France for their support in experimental protocols and in particular Dr. Diane Agay. No live animals were used for this experiment or sacrificed for the aim of this study.

References

[1] Schmitt JM. Optical coherence tomography (OCT): a review. IEEE J Sel Top Quantum Electron 1999;5:1205–15. http://dx.doi.org/10.1109/2944.796348.
[2] Webb RH, Hughes GW, Delori FC. Confocal scanning laser ophthalmoscope. Appl Opt 1987;26:1492. http://dx.doi.org/10.1364/AO.26.001492.
[3] Elliott JC, Dover SD. X-ray microtomography. J Microsc 1982;126:211–3. http://dx.doi.org/10.1111/j.1365-2818.1982.tb00376.x.
[4] Anastasio MA, La Riviere P. Emerging imaging technologies in medicine; 2012.
[5] Keyriläinen J, Fernández M, Karjalainen-Lindsberg M-L, Virkkunen P, Leidenius M, von Smitten K, et al. Toward high-contrast breast CT at low radiation dose. Radiology 2008;249:321–7.
[6] Bravin A, Coan P, Suortti P. X-ray phase-contrast imaging: from pre-clinical applications towards clinics. Phys Med Biol 2013;58:R1–35. http://dx.doi.org/10.1088/0031-9155/58/1/R1.

[7] Gasilov S, Mittone A, Brun E, Bravin A, Grandl S, Coan P. On the possibility of quantitative refractive-index tomography of large biomedical samples with hard X-rays. Biomed Opt Express 2013;4:1512–8. http://dx.doi.org/10.1364/BOE.4.001512.

[8] Kelly ME, Coupal DJ, Beavis RC, Schultke E, Romanchuk K, Juurlink BHJ, et al. Diffraction-enhanced imaging of a porcine eye. Can J Ophthalmol 2007;42:731–3. http://dx.doi.org/10.1139/i07-132.

[9] Yin H, Huang Z, Wang Z, Liu Z, Li Y. Zhu P [Application research of DEI technique based on synchrotron X-ray source in imaging rabbit eyeball in vitro]. Zhonghua Yi Xue Za Zhi 2010;90:777–81.

[10] Hoshino M, Uesugi K, Yagi N, Mohri S, Regini J, Pierscionek B. Optical properties of in situ eye lenses measured with X-ray Talbot interferometry: a novel measure of growth processes. PLoS One 2011;6. http://dx.doi.org/10.1371/journal.pone.0025140.

[11] Ivanishko Y, Bravin A, Kovalev S, Lisutina P, Lotoshnikov M, Mittone A, et al. Feasibility study of the 3D visualization at high resolution of intra-cranial rabbit eyes with X-ray CT phase-contrast imaging. Invest Ophthalmol Vis Sci 2017;58. http://dx.doi.org/10.1167/iovs.17-22273.

[12] Horng A, Brun E, Mittone A, Gasilov S, Weber L, Geith T, et al. Cartilage and soft tissue imaging using X-rays: propagation-based phase-contrast computed tomography of the human knee in comparison with clinical imaging techniques and histology. Invest Radiol 2014;49:627–34. http://dx.doi.org/10.1097/RLI.0000000000000063.

[13] Bukreeva I, Campi G, Fratini M, Spanò R, Bucci D, Battaglia G, et al. Quantitative 3D investigation of Neuronal network in mouse spinal cord model. Sci Rep 2017;7:41054. http://dx.doi.org/10.1038/srep41054.

[14] Mittone A, Bravin A, Coan P. Low-dose quantitative phase contrast medical CT. Meas Sci Technol 2018;29:024006. http://dx.doi.org/10.1088/1361-6501/aa9acd.

[15] Hubbell JH, Seltzer SM. Tables of X-ray mass attenuation coefficients and mass energy-absorption coefficients 1 keV to 20 MeV for elements Z = 1 to 92 and 48 additional substances of dosimetric interest; 1995. http://PhysicsNistGov/PhysRefData/XrayMassCoef/CoverHtml.

[16] Roessler A-C, Hupfer M, Kolditz D, Jost G, Pietsch H, Kalender WA. High atomic number contrast media offer potential for radiation dose reduction in contrast-enhanced computed tomography. Invest Radiol 2016;51:249–54. http://dx.doi.org/10.1097/RLI.0000000000000232.

[17] Fratini M, Bukreeva I, Campi G, Brun F, Tromba G, Modregger P, et al. Simultaneous submicrometric 3D imaging of the micro-vascular network and the neuronal system in a mouse spinal cord. Sci Rep 2015;5:8514. http://dx.doi.org/10.1038/srep08514.

[18] Henke BL, Gullikson EM, Davis JC. X-Ray Interactions: photoabsorption, scattering, transmission and reflection at E= 50–30000 eV, Z= 1–92. At Data Nucl Data Tables 1993;54:181–342.

[19] Snigirev A, Snigireva I, Kohn V, Kuznetsov S, Schelokov I. On the possibilities of x-ray phase contrast microimaging by coherent high-energy synchrotron radiation. Rev Sci Instrum 1995;66:5486. http://dx.doi.org/10.1063/1.1146073.

[20] Wilkins SW, Gureyev TE, Gao D, Pogany A, Stevenson AW. Phase-contrast imaging using polychromatic hard X-rays. Nature 1996;384:335–8.

[21] Cloetens P, Barrett R, Baruchel J, Guigay JP, Schlenker M. Phase objects in synchrotron radiation hard X-ray imaging. J Phys D Appl Phys 1996;29:133–46.

[22] Förster E, Goetz K, Zaumseil P. Double crystal diffractometry for the characterization of targets for laser fusion experiments. Krist Tech 1980;15:937–45.

[23] Chapman D, Thomlinson W, Johnston RE, Washburn D, Pisano E, Gmür N, et al. Diffraction enhanced x-ray imaging. Phys Med Biol 1997;42:2015–25. http://dx.doi.org/10.1088/0031-9155/42/11/001.

[24] Momose A, Takeda T, Itai Y, Hirano K. Phase–contrast X–ray computed tomography for observing biological soft tissues. Nat Med 1996;2:473–5. http://dx.doi.org/10.1038/nm0496-473.

[25] Pfeiffer F, Weitkamp T, Bunk O, David C. Phase retrieval and differential phase-contrast imaging with low-brilliance X-ray sources. Nat Phys 2006;2:258–61. http://dx.doi.org/10.1038/nphys265.

[26] Olivo A, Arfelli F, Cantatore G, Longo R, Menk RH, Pani S, et al. An innovative digital imaging set-up allowing a low-dose approach to phase contrast applications in the medical field [In Process Citation]. Med Phys 2001;28:169–1610.

[27] Takeda M, Ina H, Kobayashi S. Fourier-transform method of fringe-pattern analysis for computer-based topography and interferometry. J Opt Soc Am 1982;72:156.

[28] Morgan KS, Paganin DM, Siu KKW. Quantitative single-exposure x-ray phase contrast imaging using a single attenuation grid. Opt Express 2011;19:19781. http://dx.doi.org/10.1364/OE.19.019781.

[29] Russo P.E. Handbook of X-ray imaging: physics and technology; 2017.

[30] Born M, Wolf E. Principles of optics: electromagnetic theory of propagation, interference and diffraction of light. 7th ed. Cambridge; 1999.

[31] Suortti P, Fiedler S, Bravin A, Brochard T, Mattenet M, Renier M, et al. Fixed-exit monochromator for computed tomography with synchrotron radiation at energies 18–90 keV. J Synchrotron Radiat 2000;7:340–7.

[32] Mittone A, Manakov I, Broche L, Jarnias C, Coan P, Bravin A. Characterization of a sCMOS-based high-resolution imaging system. J Synchrotron Radiat 2017;24:1226–36. http://dx.doi.org/10.1107/S160057751701222X.

[33] Moosmann J, Hofmann R, Baumbach T. Single-distance phase retrieval at large phase shifts. Opt Express 2011;19:12066. http://dx.doi.org/10.1364/OE.19.012066.

[34] Hofmann R, Moosmann J, Baumbach T. Criticality in single-distance phase retrieval. Opt Express 2011;19:25881–90.

[35] Kak AC, Slaney M. Principles of computerized tomographic imaging. New York: IEEE Press; 1988.

[36] Mittone A, Baldacci F, Bravin A, Brun E, Delaire F, Ferrero C, et al. An efficient numerical tool for dose deposition prediction applied to synchrotron medical imaging and radiation therapy. J Synchrotron Radiat 2013;20:785–92.

[37] Massimi L, Fratini M, Bukreeva I, Brun F, Mittone A, Campi G, et al. Characterization of mouse spinal cord vascular network by means of synchrotron radiation X-ray phase contrast tomography. Phys Medica 2016;32:1779–84. http://dx.doi.org/10.1016/j.ejmp.2016.09.015.

[38] Ponchut C, Rigal JM, Clément J, Papillon E, Homs A, Petitdemange S. MAXIPIX, a fast readout photon-counting X-ray area detector for synchrotron applications. J Instrum 2011;6:C01069.

[39] Zhao Y, Brun E, Coan P, Huang Z, Sztrókay A, Diemoz PC, et al. High-resolution, low-dose phase contrast X-ray tomography for 3D diagnosis of human breast cancers. Proc Natl Acad Sci USA 2012;109:18290–4. http://dx.doi.org/10.1073/pnas.1204460109.

[40] Hu H. Multi-slice helical CT: scan and reconstruction. Med Phys 1999;26:5–18. http://dx.doi.org/10.1118/1.598470.

[41] Sena G, Nogueira LP, Braz D, Almeida AP, Gonzalez MS, Azambuja P, et al. Ecdysis period of *Rhodnius prolixus* head investigated using phase contrast synchrotron microtomography. Phys Medica 2016;32:812–7. http://dx.doi.org/10.1016/j.ejmp.2016.05.051.

[42] Stampanoni M, Groso A, Isenegger A, Mikuljan G, Chen Q, Bertrand A, et al. Trends in synchrotron-based tomographic imaging: the SLS experience. In: Bonse U, editor. vol. 6318, International Society for Optics and Photonics; 2006, p. 63180M. doi:10.1117/12.679497.